


## Article

# On the Effect of CO<sub>2</sub> on Seismic and Ultrasonic Properties: A Novel Shale Experiment

Stian Rørheim<sup>1</sup>, Mohammad Hossain Bhuiyan<sup>2</sup> , Andreas Bauer<sup>3</sup> and Pierre Rolf Cerasi<sup>2,\*</sup>

<sup>1</sup> Department of Geoscience and Petroleum, Norwegian University of Science and Technology (NTNU), NO-7034 Trondheim, Norway; stian.rorheim@ntnu.no

<sup>2</sup> SINTEF Industry, NO-7465 Trondheim, Norway; Mohammad.Bhuiyan@sintef.no

<sup>3</sup> Aker BP, NO-7011 Trondheim, Norway; andreas.bauer@akerbp.com

\* Correspondence: pierrerolf.cerasi@sintef.no

**Abstract:** Carbon capture and storage (CCS) by geological sequestration comprises a permeable formation (reservoir) for CO<sub>2</sub> storage topped by an impermeable formation (caprock). Time-lapse (4D) seismic is used to map CO<sub>2</sub> movement in the subsurface: CO<sub>2</sub> migration into the caprock might change its properties and thus impact its integrity. Simultaneous forced-oscillation and pulse-transmission measurements are combined to quantify Young's modulus and Poisson's ratio as well as P- and S-wave velocity changes in the absence and in the presence of CO<sub>2</sub> at constant seismic and ultrasonic frequencies. This combination is the laboratory proxy to 4D seismic because rock properties are monitored over time. It also improves the understanding of frequency-dependent (dispersive) properties needed for comparing in-situ and laboratory measurements. To verify our method, Draupne Shale is monitored during three consecutive fluid exposure phases. This shale appears to be resilient to CO<sub>2</sub> exposure as its integrity is neither compromised by notable Young's modulus and Poisson's ratio nor P- and S-wave velocity changes. No significant changes in Young's modulus and Poisson's ratio seismic dispersion are observed. This absence of notable changes in rock properties is attributed to Draupne being a calcite-poor shale resilient to acidic CO<sub>2</sub>-bearing brine that may be a suitable candidate for CCS.

**Keywords:** CO<sub>2</sub> storage; rock physics; anisotropy; dynamic acoustic properties



**Citation:** Rørheim, S.; Bhuiyan, M.H.; Bauer, A.; Cerasi, P.R. On the Effect of CO<sub>2</sub> on Seismic and Ultrasonic Properties: A Novel Shale Experiment. *Energies* **2021**, *14*, 5007. <https://doi.org/10.3390/en14165007>

Academic Editor: Joel Sarout

Received: 28 June 2021

Accepted: 12 August 2021

Published: 15 August 2021

**Publisher's Note:** MDPI stays neutral with regard to jurisdictional claims in published maps and institutional affiliations.



**Copyright:** © 2021 by the authors. Licensee MDPI, Basel, Switzerland. This article is an open access article distributed under the terms and conditions of the Creative Commons Attribution (CC BY) license (<https://creativecommons.org/licenses/by/4.0/>).

## 1. Introduction

Despite its recently gained momentum and level of awareness, how exactly mankind is supposed to overcome the challenge that is the reduction of anthropogenic carbon dioxide (CO<sub>2</sub>) in the atmosphere is still a question left unanswered. Considered an indispensable technology to reach the Paris Agreement targets among commonly proposed solutions, Carbon Capture and Storage (CCS) has manifested itself as a force to be reckoned with. The International Panel on Climate Change (IPCC) [1] defined CCS as “a process consisting of the separation of CO<sub>2</sub> from industrial and energy-related sources, transport to a storage location and long-term isolation from the atmosphere”. The feasibility of geological storage of CO<sub>2</sub> is demonstrated [2–4] but it is impossible to eliminate all pathways between the subsurface and the atmosphere due to the porous nature of rocks, let alone the wells themselves. Thus, it becomes a question of time as to whether CCS may be considered an option, as the injected CO<sub>2</sub> is supposed to remain in the subsurface for the 10<sup>4</sup> year timescales needed to avoid climate impacts [5–7]. In CCS context, geological storages are predominantly reservoir sands enveloped by impermeable shales. This configuration is the primary mechanism for ensuring secure and effective storage.

Mapping the movement of CO<sub>2</sub> in the subsurface to demonstrate its secure retention is paramount but it is uncertain whether the integrity of the seal is compromised (and to what extent) due to continued exposure to CO<sub>2</sub>. Busch et al. [8] identified storage conformance and seal integrity as key in risk of leakage determination as well as storage capacity and

injectivity limitations. Kampman et al. [7] named low permeability and capillary entry pressure as two mechanisms that retard CO<sub>2</sub> migration. Direct and indirect observations are not only possibilities but also necessities. The former is expensive and technically difficult while the latter (mostly based on seismic surveillance) is both cost-effective and non-intrusive [9]. Seismic monitoring is associated with a certain degree of ambiguity from being influenced by a multitude of factors (e.g., mineralogical composition, porosity, pore fluid, pore pressure, degree of saturation, and in-situ state of stress) [10].

When injected into a reservoir, CO<sub>2</sub> displaces the pore fluid (water or brine) and with time either dissolves into the pore fluid or remains as free CO<sub>2</sub>. It will also react to make more stable phases. Buoyancy generates a plume-like structure due to the concentration of free CO<sub>2</sub> at the reservoir-caprock interface, accompanied by a pressure difference that depends on in-situ pressure and temperature conditions [11] for a normal hydrostatic situation. Espinoza and Santamarina [11] provided a threefold explanation of plausible causes of caprock sealing capacity degradation: “(i) hydraulic fracture and fault (re)activation by reservoir overpressure, (ii) aqueous CO<sub>2</sub> diffusion into caprock water (without bulk CO<sub>2</sub> invasion) and consequent water acidification and mineral dissolution, and (iii) CO<sub>2</sub> invasion into caprock, capillary breakthrough, and CO<sub>2</sub> advection”. The primary mechanism of cause (i) is alterations in effective stress that may change the mechanical and petrophysical properties of rocks (strength, stiffness, deformation, permeability, and porosity). Cause (ii) is due to concentration gradients combined with pH being inversely proportional to CO<sub>2</sub>-dissolution, and cause (iii) is prevented when the buoyancy-induced fluid pressure is lower than the capillary entry pressure of the seal.

Other less known coupled processes that could impair the integrity of the seal include [11]: “reactivity of water dissolved in CO<sub>2</sub>, CO<sub>2</sub> intercalation in clays, changes in electrical interaction between clay particles due to water acidification and displacement by CO<sub>2</sub>, and caprock dehydration and capillary-driven volumetric contraction”. These fluid-rock reactions are ambiguous as mineral precipitation-induced self-sealing phenomena that limit the diffusion of CO<sub>2</sub> are numerically predicted, while self-enhancing mineral dissolution and porosity generation that create a continuous increase in transport properties are experimentally observed [7]. CO<sub>2</sub>-dissolution in brine has been experimentally proven to increase with pressure at given temperature and NaCl-concentration, decrease with temperature for given pressure and brine compositions, and decrease with NaCl concentration for a given temperature and pressure [12,13]. Minerals such as feldspar, calcite, and pyrite may succumb to precipitation and dissolution induced by decreasing pore fluid pH [14]. Chlorite and illite are partly transformed into smectite in the aftermath of interaction with supercritical CO<sub>2</sub> (scCO<sub>2</sub>) [15]. scCO<sub>2</sub> also impacts the swelling of shales to a greater extent than pure water and brine [16]. Clay minerals adsorb vast quantities of CO<sub>2</sub>, with Ca-exchanged smectite adsorbing the most, followed by Na-exchanged smectite, illite, and kaolinite, while the contribution from chlorite is negligible [17]. Since illite and kaolinite also adsorb CO<sub>2</sub>, adsorption must be a mineral surface phenomenon rather than an interlayer one: most adsorption tests involve powdered specimens in which the surface area in contact with CO<sub>2</sub> is significantly increased [18]. Klewiah et al. [19] recently reviewed experimental sorption studies of CO<sub>2</sub> (and CH<sub>4</sub>) in shales where the influence of organic matter, thermal maturity, kerogen type, inorganic components, moisture, and temperature are elaborated.

Uniaxial compressive strength (UCS) experiments on shales exposed to CO<sub>2</sub>-water or CO<sub>2</sub>-brine feature a reduction of Young's modulus  $E$  and Poisson's ratio  $\nu$  [16,20–25]. If only exposed to scCO<sub>2</sub>, Choi et al. [25] measured an increased Young's modulus. Tensile strength is determined by the Brazilian test, in which different shales were found to be both sensitive (decrease and increase in strength) [25–29] and insensitive (constant strength) [30] to CO<sub>2</sub> exposure. The common denominator in both experiment types is that the specimens are submitted to mechanical testing at ambient temperature and pressure conditions after being exposed to CO<sub>2</sub>. Reintroducing specimens to ambient conditions post CO<sub>2</sub> exposure could influence their mechanical properties due to microstructure damages caused by

CO<sub>2</sub> exsolution [31]. It is thus difficult to attribute any observed changes in Young's modulus and Poisson's ratio to the effect of CO<sub>2</sub> alone. Triaxial compression tests (UCS plus confining and pore pressure) are able to counter these artifacts by maintaining constant temperatures and pressure close to in-situ conditions. Decreasing triaxial strength [26] and increasing Young's modulus [29] are also measured with increasing scCO<sub>2</sub> exposure time. Agofack et al. [32] detected a decrease in Young's modulus and Poisson's ratio for a triaxial compressed Draupne Shale. Their results are however inconclusive due to procedural flaws related to limited number of measurements that made statistical analysis difficult, and CO<sub>2</sub> exsolution that could affect the undrained bulk modulus via pore fluid compressibility caused by decreasing pore pressure during loading. Choi et al. [25], Al-Ameri et al. [33], Elwegaa et al. [34] measured decreasing ultrasonic P- and S-wave velocities post-CO<sub>2</sub> exposure which the two latter converted to decreasing dynamic Young's modulus assuming isotropy. Lebedev et al. [35] considered anisotropy for their shaley sandstones that also decreased in P-wave velocity upon scCO<sub>2</sub> injection into brine-occupied pore space. Consistent with their compressive and tensile strength results, Choi et al. [25] measured increasing P-wave velocity if only exposed to scCO<sub>2</sub>. Dewhurst et al. [18] reiterated that shale dehydration may alter the rock properties being measured: strength and elastic properties (Young's modulus and Poisson's ratio) from triaxial testing are particularly impacted by pore fluid loss. Bhuiyan et al. [31], Fatah et al. [36] neatly summarized CO<sub>2</sub>-shale interactions in terms of CCS implications.

Upon being recognized as a potential CCS candidate due to its extension over planned CCS reservoirs, Draupne's mechanical properties are studied in the absence and presence of CO<sub>2</sub> [32,37–39]. Draupne Shale is associated with high capillary sealing (from a permeability viewpoint) but Skurtveit et al. [37] questioned its formation and sealing capacity by indirect tensile strength and undrained shear strength experiments. Zadeh et al. [38] observed increasing P- and S-wave velocities but decreasing Thomsen's parameters with increasing mean effective stress. To the best of our knowledge, Draupne's mechanical properties are unprobed at seismic frequencies. It is also unexplored at different fluid exposure phases (including CO<sub>2</sub> exposure) over an elongated period of time within the same experiment.

Most studies involve post-CO<sub>2</sub>-interaction experiments at ambient conditions devoid of CO<sub>2</sub> in its experimental condition at either subseismic or ultrasonic frequencies. There is a paucity of studies involving CO<sub>2</sub> experiments under continuous in situ conditions at seismic frequencies. We present a method to monitor the mechanical responses of a specimen exposed to CO<sub>2</sub> over an elongated period of time using the forced-oscillation (FO) and pulse-transmission (PT) techniques. PT is the dominant dynamic technique but FO and resonant bar (RB) studies also exist albeit limited to sandstones exposed to CO<sub>2</sub> [40–45]. The novelty of our approach is that our specimen is exposed to three different fluids while confined under continuous stress, pressure, and temperature regimes. We attempt to answer the question whether CO<sub>2</sub> changes the mechanical properties of a caprock and thus present a risk for efficient, long-term containment in the reservoir below. To this end, we determine whether Draupne Shale is suitable candidate for CCS by monitoring Young's modulus and Poisson's ratio at seismic as well as P- and S-wave velocities at ultrasonic frequencies over 575 h. Since no significant changes are observed, Draupne Shale may be a suitable candidate.

## 2. Theory

### 2.1. Anisotropy

Anisotropic or isotropic is the material whose elastic properties change or do not change with direction. Anisotropy in shales is caused by the alignment of minerals (particularly clays). The number of independent stiffnesses for anisotropic rocks exceeds the two required to describe isotropic rocks: shales are commonly considered to be transversely isotropic (TI) which increases this number to five [10]. Hooke an theory relates

stress  $\vec{\sigma} = (\sigma_{11} \sigma_{22} \sigma_{33} \sigma_{23} \sigma_{13} \sigma_{12}) \equiv (\sigma_1 \sigma_2 \sigma_3 \sigma_4 \sigma_5 \sigma_6)$  and strain  $\vec{\epsilon} = (\epsilon_{11} \epsilon_{22} \epsilon_{33} \epsilon_{23} \epsilon_{13} \epsilon_{12}) \equiv (\epsilon_1 \epsilon_2 \epsilon_3 \epsilon_4 \epsilon_5 \epsilon_6)$  (notation for TI symmetry by Voigt [46]) via “ut tensio, sic vis” [47] as

$$\underbrace{\begin{pmatrix} \sigma_1 \\ \sigma_2 \\ \sigma_3 \\ \sigma_4 \\ \sigma_5 \\ \sigma_6 \end{pmatrix}}_{\vec{\sigma}} = \underbrace{\begin{pmatrix} C_{11} & C_{11} - 2C_{66} & C_{13} & 0 & 0 & 0 \\ C_{11} - 2C_{66} & C_{11} & C_{13} & 0 & 0 & 0 \\ C_{13} & C_{13} & C_{33} & 0 & 0 & 0 \\ 0 & 0 & 0 & C_{44} & 0 & 0 \\ 0 & 0 & 0 & 0 & C_{44} & 0 \\ 0 & 0 & 0 & 0 & 0 & C_{66} \end{pmatrix}}_{\vec{C}} \underbrace{\begin{pmatrix} \epsilon_1 \\ \epsilon_2 \\ \epsilon_3 \\ 2\epsilon_4 \\ 2\epsilon_5 \\ 2\epsilon_6 \end{pmatrix}}_{\vec{\epsilon}}, \quad (1)$$

with  $C_{11}$ ,  $C_{13}$ ,  $C_{33}$ ,  $C_{44}$ , and  $C_{66}$  being the five independent stiffnesses. Triaxial cells generate biaxial stress conditions ( $\sigma_z > \sigma_x = \sigma_y$ ) with confining pressure  $P_f = \sigma_x = \sigma_y$  and axial stress  $\sigma_z$ , which enable the determination of all five stiffnesses if three differently oriented samples are considered. To this end, 0 and 90° specimens are required, whereas the third specimen orientation is not required to be 45° but often is for consistency. Thomsen [48] defined three anisotropic parameters to simplify anisotropy

$$\epsilon = \frac{C_{11} - C_{33}}{2C_{33}}, \quad (2)$$

$$\gamma = \frac{C_{66} - C_{44}}{2C_{44}}, \quad (3)$$

$$\delta = \frac{(C_{13} + C_{44})^2 - (C_{33} - C_{44})^2}{2C_{33}(C_{33} - C_{44})}, \quad (4)$$

where  $\epsilon$  and  $\gamma$  denote P- and S-wave anisotropy, while  $\delta$  is referred to as the moveout parameter (a critical factor that depends on the shape of the wavefronts).  $\epsilon = \gamma = \delta = 0$  implies isotropy for these dimensionless, ratio-based parameters.

## 2.2. Cole–Cole Model

Ref. [49] extended the Cole–Cole model [50] from the realm of dielectric constants of liquids to the realm of viscoelastic rocks with a distribution of relaxation times

$$M^* = M_R + iM_I, \quad (5)$$

$$M_R = M_0 + \frac{M_\infty - M_0}{2} \left( 1 + \frac{\sinh((1 - \alpha)x)}{\cosh((1 - \alpha)x) + \sin\left(\frac{\alpha\pi}{2}\right)} \right), \quad (6)$$

$$M_I = \frac{\frac{M_\infty - M_0}{2} \cos\left(\frac{\alpha\pi}{2}\right)}{\cosh((1 - \alpha)x) + \sin\left(\frac{\alpha\pi}{2}\right)}, \quad (7)$$

with  $M_R$  and  $M_I$  being the real and imaginary parts of the complex modulus  $M^*$ ;  $M_0$  and  $M_\infty$  its low- and high-frequency (or relaxed and unrelaxed) limits. Not to be confused with any specific modulus,  $M$  is a general modulus.  $x = \ln(\omega\tau_0)$  with  $\omega$  being the angular frequency and  $\tau_0$  being the characteristic time.  $\alpha \in [0, 1]$  describes the width of the distribution of relaxation times.  $\alpha = 0$  reduces it to the underlying Debye model [51].  $M$  is the magnitude of the modulus and  $Q_M^{-1}$  is its corresponding attenuation

$$M = \sqrt{M_R^2 + M_I^2}, \quad (8)$$

$$Q_M^{-1} = \frac{\Im(M)}{\Re(M)} = \frac{M_I}{M_R}. \quad (9)$$

If the application of the Cole–Cole model for anisotropic rocks is a valid assumption (the anelasticity satisfies the Kramers–Kronig relations (KKR) [52,53], the system is linear, and the attenuation can be described by a single mechanism), it is possible to use

this model to perform a qualitative fit based on mathematically solving a least-squares function [49,54,55].

### 3. Materials and Methods

The versatile nature of our apparatus accommodates simultaneous FO and PT measurements at seismic and ultrasonic frequencies, respectively. Strain amplitudes between  $10^{-7}$  and  $10^{-6}$  apply not only to FO and the field but also to PT [56,57].

#### 3.1. Mechanical Measurements

Szewczyk et al. [58] described the apparatus as “a technique for the complete characterization of the frequency-dependent elastic properties of anisotropic rocks under stress”. It was designed to accommodate specimens with 2.54 cm diameter and 5.08 cm length. To this end, (i) quasistatic specimens deformations, (ii) Young’s modulus and Poisson’s ratio [49,54] at seismic frequencies, and (iii) P- and S-wave velocities [59–62] at ultrasonic frequencies are measurable at different temperature, stress, and pressure conditions (Figure 1). Stress and pressure are controlled by an electromechanical frame (MTS Criterion C45 300 kN) and high-accuracy pumps (Vindum VP-Series), respectively. A CO<sub>2</sub> flow loop (described in Section 3.4) enabled CO<sub>2</sub> effects to be studied [44,45].

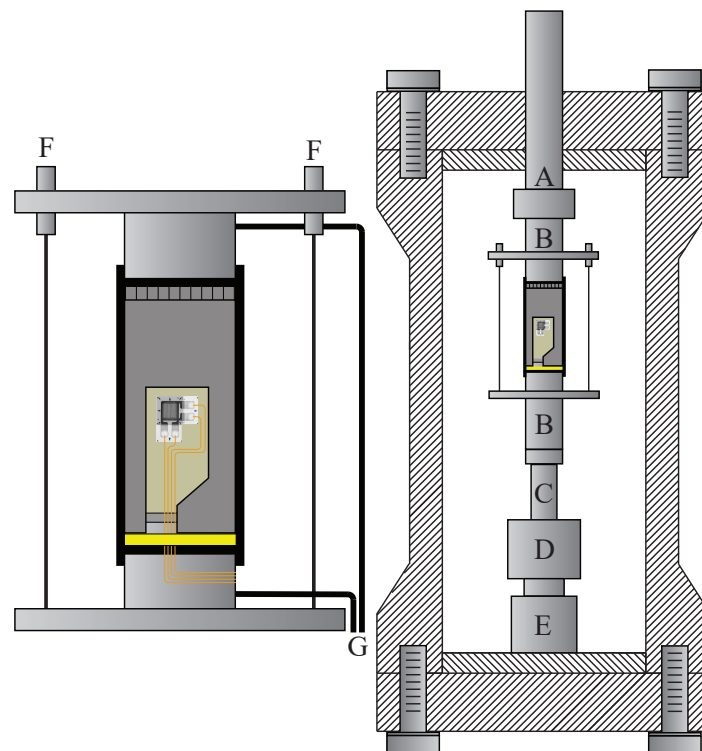


**Figure 1.** Apparatus schematics with letters indicating the different components: piston (A), top and bottom endcaps with embedded P- and S-wave transducers (B), piezoelectric force sensor (C), piezoelectric actuator (D), internal load cell (E), linear variable displacement transducers (LVDTs) (F), and pore fluid lines (G). Added to that, the specimen (regular and superimposed) with attached strain gauges (but without any letter indicators) mediates two sintered plates, as well as being covered by a mesh to ensure pore pressure equilibrium inside the enclosing rubber sleeve. Lozovyi and Bauer [63] further elaborate on the different components.

#### 3.1.1. Forced-Oscillation (FO) Measurements

Five Stanford Research SR850 lock-in amplifiers (internal sampling rate of 256 kHz) measure amplitudes and phases of harmonic signals. Uniaxial-stress modulations are generated by a piezoelectric actuator (PI P-235.1S) controlled by a sinusoidal reference signal from one lock-in amplifier and amplified by a voltage amplifier (PI E-421). A piezoelectric

force sensor (Kistler 9323AA combined with Kistler 5015A) measures the resulting force signal returned to the lock-in amplifier which determines its amplitude and phase shift relative to the reference signal. Four biaxial strain gauges (Micro-Measurements CEA-06-125WT-350) with eight different gauge elements (four axial and four radial) are connected to four unbalanced Wheatstone bridges [64]. Each Wheatstone bridge is connected to two equidistantly strain gauges elements  $180^\circ$  apart (Figure 2) which averages the signals from both. Four lock-in amplifiers (two axial and two radial) measure amplitudes and phase shifts of the resulting strain signals relative to the reference signal. Axial stress  $\sigma_{ax}$  plus axial and radial strains ( $\epsilon_x$  is  $\epsilon_{ax}$  or  $\epsilon_{rad}$ ) are then

$$\sigma_{ax} = \frac{F}{A}, \quad (10)$$

$$\epsilon_x = \frac{2B_x}{V_{in}G_F}, \quad (11)$$

where  $F$ ,  $A$ ,  $B_x$ ,  $V_{in}$ , and  $G_F$  are force (amplitude  $B_f$  multiplied with sensitivity  $F_S$ ), cross-sectional area, measured voltage signals across the unbalanced Wheatstone bridges ( $B_x$  is total axial  $B_{ax}$  or radial  $B_{rad}$  amplitude), input activation voltage, and gauge factor, respectively. Note that circumferential strain is equal to radial strain ( $\epsilon_\theta = \epsilon_{rad}$ ) within the isotropic plane of an TI medium:  $\epsilon_{rad}$  and  $B_{rad}$  are used for simplicity. Averaging multiple strain measurements at different positions approximates the bulk mechanical properties of a rock [65]. All recordings from the lock-in amplifier are simultaneously sampled by an in-house acquisition software designed to detect stability (within a pre-defined tolerance) and average up to 50 recordings.

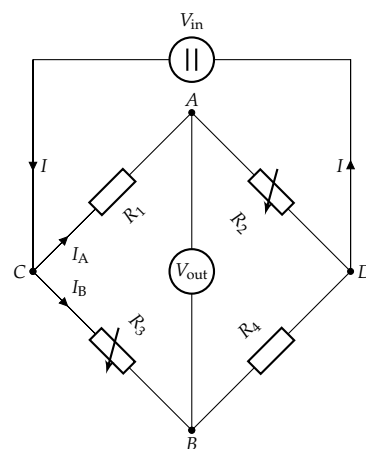


**Figure 2.** Diagonally configured Wheatstone bridge with two variable resistors (strain gauges)  $R_2$  and  $R_3$  and two passive resistors  $R_1$  and  $R_4$ . This configuration measures normal strain independently of bending strain.  $V_{out} = B_x$  in Equation (11).

Young's modulus  $E = \sigma_{ax}/\epsilon_{ax}$  [66] and Poisson's ratio  $\nu = -\epsilon_{rad}/\epsilon_{ax}$  [67] as electrical signals transformed into mechanical responses become

$$E = \frac{B_f F_S V_{in} G_F}{2A B_{ax}}, \quad (12)$$

$$\nu = -\frac{B_{rad}}{B_{ax}}, \quad (13)$$

in which  $E = E_V$  and  $\nu = \nu_{VH}$  since only a  $0^\circ$  specimen is considered (Figure 3). Equation (12) combines Equations (10) and (11) to provide the total amplitude  $E \equiv E_R + iE_I$  from the stress–strain hysteresis loop (e.g., Lakes [68]). However, since phase shifts for shales are small [69–72],  $E \approx E_R$ . Since the force sensor and strain gauges differ in elec-

tronic circuitry, electronics-induced phase shifts are greater than the rock specimen-induced ones [58]. Attempts to use an aluminum standard as force sensor [54] with similar circuitry were temporarily abandoned [73,74] until a design flaw causing unreliable phase measurements due to minor misalignments [75] was ultimately discovered [76].

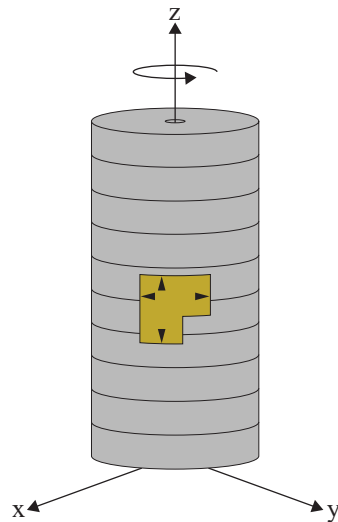


**Figure 3.** Geometry of a  $0^\circ$  specimen assuming TI symmetry featuring a biaxial strain gauge with triangles indicating measurement directions.

### 3.1.2. Pulse-Transmission (PT) Measurements

Four P- and S-wave piezoceramics (500 kHz) integrated in both endcaps measure P- and S-wave velocities based on the time of flight principle

$$V_{x_0} = \frac{L}{\underbrace{t - t_0}_{\Delta t}}, \quad (14)$$

where  $L$  is the specimen length,  $t$  is the travel time, and  $t_0$  is the system travel time. The ultrasonic signals are acquired by a system comprising a signal generator (Agilent 33220A), an amplifier (T&C Power Conversion AG 1017L), a switch unit (Agilent 34970A), and an oscilloscope (Tektronix TDS3012B) that are connected to a computer and controlled by another in-house software that also stores the data. The sampling frequency is 10 MHz. To improve the signal-to-noise ratio, the amplified ( $\sim 50$  dB) waveforms are averaged (64 times) by the oscilloscope.  $V_{x_0}$  is either  $V_{P_0}$  or  $V_{S_0}$  which combined with density  $\rho$  yields

$$C_{33} = \rho V_{P_0}^2, \quad (15)$$

$$C_{44} = \rho V_{S_0}^2, \quad (16)$$

with 0 implying the considered  $0^\circ$  specimen (Figure 3) and its corresponding stiffnesses  $C_{33}$  and  $C_{44}$ . Figure 4 exemplifies P- and S-waveforms at 500 kHz. Szewczyk et al. [77] described the arrival picking procedure in which aluminum 7075 was used for calibration purposes. The S-wave signal is disfigured by faster P-waves that spawn from initial S-waves at every acoustic impedance interface. There is thus more ambiguity in picking the first S- than P-wave arrivals.

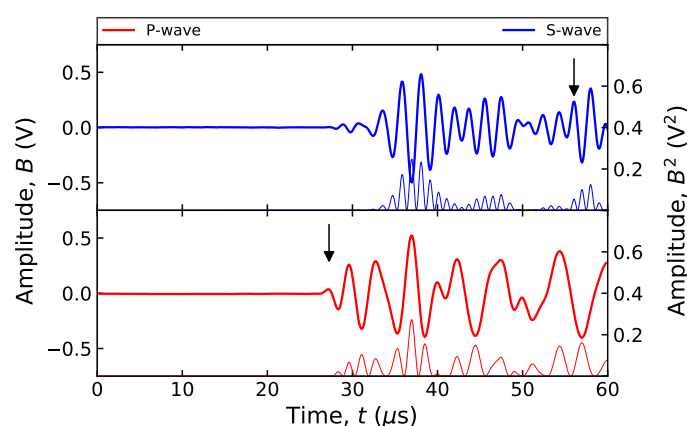


**Figure 4.** Examples of PT measured P- (red) and S-waveform (blue) amplitudes  $R$  (thick) and  $R^2$  (thin) versus time  $t$ , respectively. Arrows indicate first arrivals.

### 3.2. Draupne Shale

In the ongoing large-scale CCS demonstration project in Norway, several potential storage reservoirs have been chosen in the vicinity of the Troll gas field. Draupne Shale is the caprock in this area [78]. The specimen used herein originates from well 16/8-3S within the Ling Depression located in the central North Sea [32,37–39]. Considered an anisotropic and homogeneous shale, Zadeh et al. [38] described the Draupne Formation while investigating specimens from the same well as this study. Tables 1 and 2 tabulate Draupne’s pre-CO<sub>2</sub> exposure mineralogical composition and physical properties. Extracted from a 13.0 cm interval between 2574.86 and 2576.99 m depth, the specimen experienced minimum exposure to ambient conditions due to our accelerated mounting procedure. Diffusion time was reduced by drilling a 1.50 mm hole along its axis at the center of the specimen that also reduced the diffusion length from 12.7 to ~6 mm. Since we measure local strains at the surfaces of the specimen, we assume that this action has negligible effect on the overall stiffness of the material.

**Table 1.** Mineralogical composition of Draupne Shale from X-ray diffraction (XRD) analysis.

Mineralogy	Content (wt.%)
Quartz	15.1
K-Feldspar	3.00
Plagioclase	2.70
Chlorite	2.30
Kaolinite	16.7
Mica-Illite	13.6
Calcite	0.80
Illite-Smectite	42.9
Siderite	0.20
Dolomite	0.60
Pyrite	2.10

**Table 2.** Physical properties of Draupne Shale provided by Skurtveit et al. [37] and SINTEF.

Parameter(s)	Units	Values
Porosity	%	12.5
Permeability	nD	3.20
Grain density	g/cc	2.51
Pore throat size	nm	9.00
Pore fluid composition	% NaCl	3.60
Water content	%	6.40



### 3.3. Experimental Protocol

Although our apparatus is able to perform measurements at elevated temperatures [79], the current experiment occurred at room temperature to concentrate on CO<sub>2</sub>-driven mechanisms that may influence the mechanical properties of our specimen. Confining pressure  $P_c$ , pore pressure  $P_f$ , and axial stress  $\sigma_{ax}$  were kept constant, respectively, at 20, 10, and 12 MPa from the outset and throughout (Figure 5). Adequate system–specimen coupling is ensured by a finite deviatoric stress ( $\sigma_{ax} - P_c = 2$  MPa). The specimen was left to consolidate while LVDTs and strain gauges were constantly monitored and analyzed before initiating FO. Three fluid exposure phases are implemented: constant pressure without (closed system for the specimen to consolidate (Phase (i))) and with fluid flow (open system regulated by a back pressure connected to a pump administrating brine (Phase (ii)) or the CO<sub>2</sub> flow loop (Phase (iii))) at 0.025 mL/min. Fluids are distributed around the specimen by a surrounding mesh, two sintered plates at each specimen–endcap interface, and the hole at its center. In other words, there is no flow through the specimen but instead around it and within the hole. For all intents and purposes, roman numbering indicates the respective phases of flow in terms of the previously defined (i), (ii), and (iii) in all graphs with time as the x-axis (exemplified by Figure 5). Three dynamic test procedures were planned and executed with the objectives being to (a) monitor the elastic response of our specimen at a constant frequency with time, (b) complete dispersion characterization tests with frequency before and after the former, and (c) PT recordings at ultrasonic frequencies:

- Frequency sweeps were performed once the specimen was adequately consolidated (by analyzing deformation) in order to identify the optimal frequency to be used for the duration of the experiment. 25 Hz was proven to generate the optimum signal with a sampling interval of 60 s to constrain the data size.
- A total of three dispersion tests (full frequency sweeps from 1 to 144 Hz) at two different exposure phases were sequentially conducted: (i) and (ii) during consolidation in Phase (i), and (iii) at the of end of the experiment in Phase (iii).
- A third test was also simultaneously executed as P- and S-wave ultrasonic signals were recorded every 900 s during the entirety of the test.

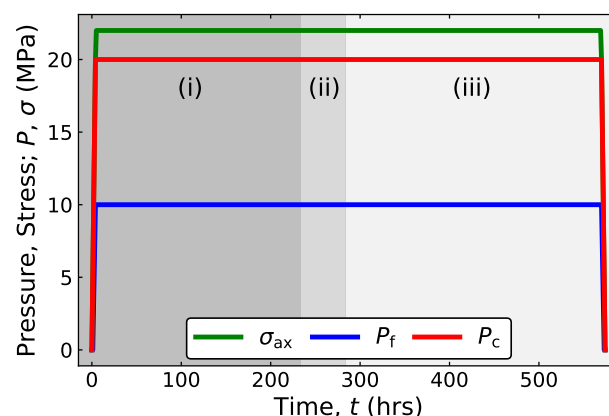


**Figure 5.** Confining pressure  $P_c$ , pore pressure  $P_f$ , and axial stress  $\sigma_{ax}$  versus time  $t$ . Roman numbering combined with the grayscale background indicates the respective phases of fluid exposure: Phase (i), Phase (ii), and Phase (iii).

### 3.4. CO<sub>2</sub> Flow Loop

The CO<sub>2</sub> flow loop system comprises a CO<sub>2</sub> container (13.4 L capacity), an accumulator (1 L capacity), a mixing unit (1 L capacity), two pumps (Quizix and vacuum), as well as three Eurotherm temperature controllers (Figure 6) [44,45]. Integrated in the accumulator is a movable seal membrane that separates CO<sub>2</sub> in the lower part from oil in the upper part. The mixing unit was filled with 80% brine of 3.6 wt% NaCl concentration. CO<sub>2</sub> exsolution during wave-induced pressure changes is prevented by heating the mixing



(i) is categorized into two dominant features based on the expansion rate of the specimen: rapid expansion from 4 to 70 h after the desired pressure and stress levels are enforced, and slow expansion after 70 h until the initiation of the next phase. Phase (ii) is similar to Phase (i) in trend but not in amplitude since the specimen also initially expands before it eventually slows down again (at a lower rate than the previous phase). Phase (iii) saw an initial decrease in  $\epsilon_{ax}$  as CO<sub>2</sub> was introduced at 283 h. Compaction turned into expansion at 320 h, whereupon the specimen expanded at a continuously decreasing rate until the end of the experiment.

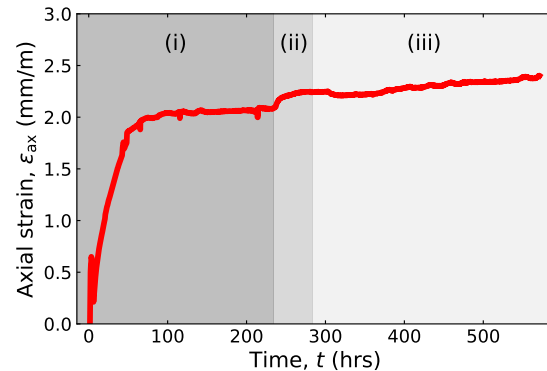


**Figure 7.** Axial strain  $\epsilon_{ax}$  versus time  $t$ . Roman numbering combined with the grayscale background indicates the respective phases of fluid exposure: Phase (i), Phase (ii), and Phase (iii).

Figure 8 features Young's modulus  $E_V$  and Poisson's ratio  $\nu_{VH}$  as a function of time: (a) includes the entire experiment while (b) is superimposed from 220 to 330 h with narrower y-axes. As the signals are stabilized with time (Figure 8b), subsequent phases are sequentially initiated. Phase (i) is primarily used for stability and as reference to determine changes in mechanical properties. Phase (ii) introduced at approximately 234 h decreased  $E_V$  by 1.57%. Phase (iii) introduced at 283 h had an initial stiffening effect ( $E_V$  increased by 1.04%) for the first 80 h after influx before plateauing at 364 h with approximately constant  $E_V$  until the end. Poisson's ratio  $\nu_{VH}$  remained resilient to the different phases as a function of time without any noteworthy changes. Figure 9 includes ultrasonic P- and S-wave velocities at 500 kHz recorded every 900 s for the entirety of the test. Despite an accelerated reduction after introducing the brine–CO<sub>2</sub> combination, a proclivity towards steady decline of both  $V_{P_0}$  and  $V_{S_0}$  is the noteworthy feature during all three phases.

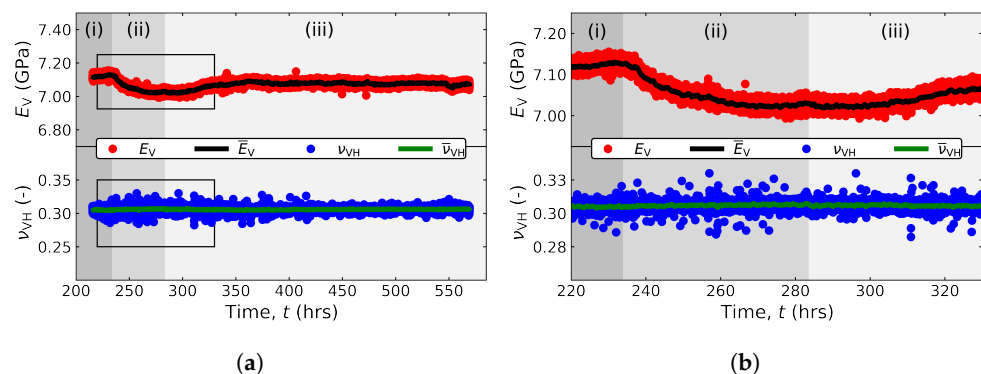


**Figure 8.** FO measured Young's modulus ( $E_V$  and its averaged namesake  $\bar{E}_V$ ) and Poisson's ratio ( $\nu_{VH}$  and its averaged namesake  $\bar{\nu}_{VH}$ ) versus time  $t$  at 25 Hz. Roman numbering combined with the grayscale background indicates the respective phases of fluid exposure: Phase (i), Phase (ii), and Phase (iii). Rectangles in (a) indicate x- and y-limits in (b). Fifty measurements were averaged.

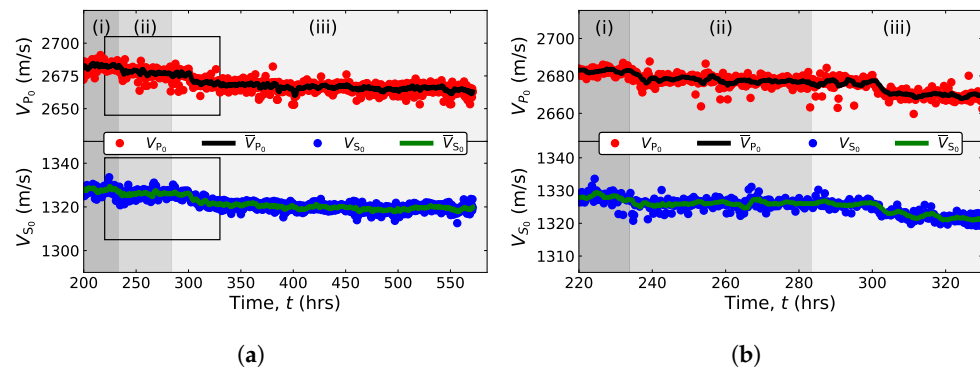


**Figure 9.** PT measured P-wave velocity ( $V_{P_0}$  and its averaged namesake  $\bar{V}_{P_0}$ ) and S-wave velocity ( $V_{S_0}$  and its averaged namesake  $\bar{V}_{S_0}$ ) versus time  $t$  at 500 kHz. Roman numbering combined with the grayscale background indicates the respective phases of fluid exposure: Phase (i), Phase (ii), and Phase (iii). Rectangles in (a) indicate x- and y-limits in (b). Rectangles in (a) indicate x- and y-limits in (b). Ten measurements were averaged.

Dispersion is a phenomenon that is a common feature in fluid-saturated rocks. DT#1, DT#2, and DT#3 (dispersion tests numbering from 1 to 3) were executed at 43, 64, and 570 h, respectively. In other words, DT#1 and DT#2 occurred at the initial stage of Phase (i) plus DT#3 at the tail-end of Phase (iii). No dispersion measurements were conducted during Phase (ii) in order to continuously focus on changes in  $E_V$  and  $\nu_{VH}$  at 25 Hz. Despite  $E_V$  being reduced in terms of magnitude (DT#1 eclipses both DT#2 and DT#3) as a function of time, regression reveals that seismic dispersion appears unaffected by  $\text{CO}_2$  exposure, with the increase from 1 to 144 Hz being within 2.41–2.88%. Figure 10b shows Poisson's ratio  $\nu_{VH}$  as a function of frequency without any noteworthy aspects in need of elaboration beyond the evident continuity.

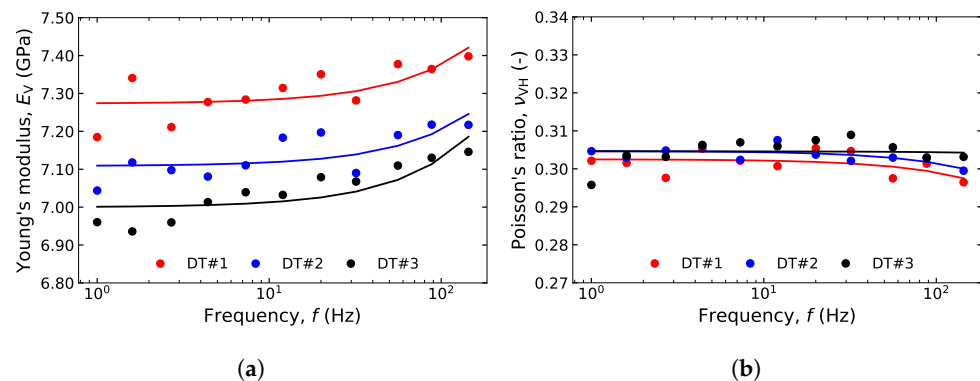


**Figure 10.** FO measured Young's modulus  $E_V$  (a) and Poisson's ratio  $\nu_{VH}$  (b) versus frequency  $f$  with their respective regression lines at 43, 64, and 570 h corresponding to DT#1, DT#2, and DT#3.

## 5. Discussion

### 5.1. Analysis

Cole–Cole modelling is a mathematical solution to a physical problem that estimates dispersive properties at unprobed frequencies. Figure 11 combines these assumptions with a least-squares-based joint-fit routine [79,80] which uses  $C_{11}$ ,  $C_{13}$ ,  $C_{33}$ ,  $C_{44}$ , and  $C_{66}$  at  $f_0$  and  $f_\infty$  plus Cole–Cole's  $f_c$  and  $\alpha$  as fit parameters. Fit ambiguity is related to the limited input data: the more inputs, the less ambiguity. Since there are no common parameters measured at both seismic and ultrasonic frequencies, the model is constrained by assuming  $E_H > E_{45} > E_V$  and  $0 < \nu_{HH} < \nu_{HV}$  to be true [81]. Figure 11 features (until now undefined) anisotropic Young's moduli  $E_V$ ,  $E_{45}$ , and  $E_H$ , Poisson's ratios  $\nu_{VH}$ ,  $\nu_{HV}$ , and  $\nu_{HH}$ , and P- and S-wave velocities  $V_{x\theta}$  ( $x$  is P or S depending on  $\pm$  being + or – and  $\theta$  is 0, 45, or 90)

$$E_V = C_{33} - \frac{C_{13}^2}{(C_{11} - C_{66})} = \frac{(C_{11} - C_{66})C_{33} - C_{13}^2}{C_{11} - C_{66}}, \quad (17)$$

$$E_{45} = 4 \left( \frac{1}{E_V} + \frac{1}{E_H} + \frac{1}{C_{44}} - \frac{C_{13}}{\underbrace{(C_{11} - C_{66})C_{33} - C_{13}^2}_{2 \frac{\nu_{VH}}{E_H}}} \right)^{-1}, \quad (18)$$

$$E_H = \frac{4C_{66}((C_{11} - C_{66})C_{33} - C_{13}^2)}{C_{11}C_{33} - C_{13}^2}, \quad (19)$$

$$\nu_{VH} = \frac{C_{13}}{2(C_{11} - C_{66})}, \quad (20)$$

$$\nu_{HV} = \frac{2C_{66}C_{13}}{C_{11}C_{33} - C_{13}^2}, \quad (21)$$

$$\nu_{HH} = \frac{(C_{11} - 2C_{66})C_{33} - C_{13}^2}{C_{11}C_{33} - C_{13}^2}, \quad (22)$$

$$V_{x\theta} = \sqrt{\frac{C_{11} \sin^2 \theta + C_{33} \cos^2 \theta + C_{44} \pm \sqrt{((C_{11} - C_{44}) \sin^2 \theta - (C_{33} - C_{44}) \cos^2 \theta)^2 + 4(C_{13} + C_{44})^2 \sin^2 \theta \cos^2 \theta}}{2\rho}}, \quad (23)$$

where  $C_{11}$ ,  $C_{13}$ ,  $C_{33}$ ,  $C_{44}$ , and  $C_{66}$  are the predefined stiffnesses. Figure 11 also includes (absolute value) Cole–Cole modeled attenuation (dashed lined) to compliment dispersion (solid lines) but remains unelaborated due unreliable phase measurements (caused by minor misalignments [75]) that were later resolved [76,80].

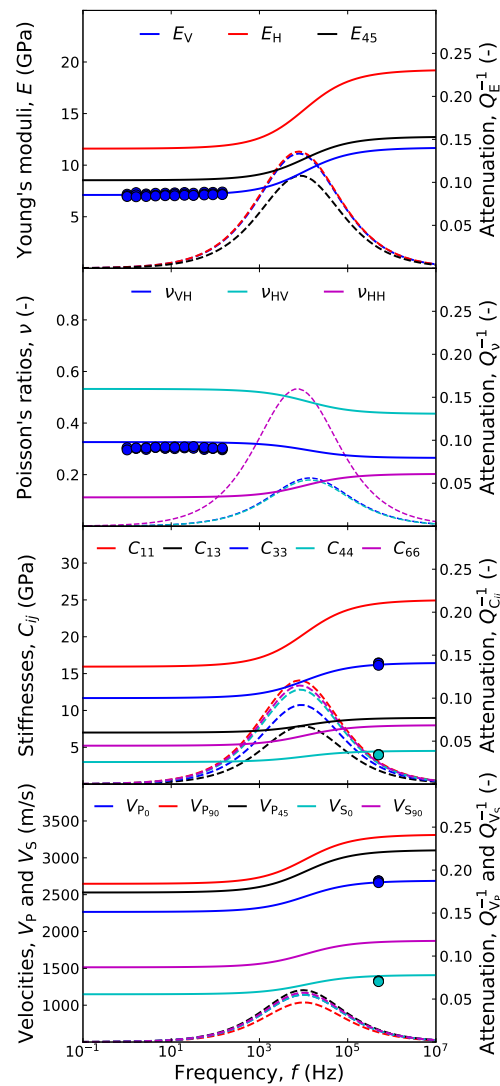


**Figure 11.** Young’s moduli ( $E_V$ ,  $E_H$ , and  $E_{45}$ ), Poisson’s ratios ( $\nu_{VH}$ ,  $\nu_{HV}$ , and  $\nu_{HH}$ ), stiffnesses ( $C_{11}$ ,  $C_{13}$ ,  $C_{33}$ ,  $C_{44}$ , and  $C_{66}$ ), and P- and S-wave velocities ( $V_{P_0}$ ,  $V_{P_{45}}$ ,  $V_{P_{90}}$ ,  $V_{S_0}$ , and  $V_{S_{90}}$ ) versus frequency  $f$ . Circles are measurements. Solid (dispersion) and dashed (attenuation) are modeled.

## 5.2. Interpretation

Achieving full saturation is challenging for any field specimens submitted to laboratory experiments. Shale specimens expand when exposed to brine irrespective of the activity of the exposed fluid and pore fluid [82]. Figure 7 shows initial expansion (at ambient conditions) explained by the adsorption of water. Despite briefly being mechanically compacted, the specimen begins to swell again probably due to continued adsorption of water. The specimen eventually becomes fully saturated and the swelling rate subsides at approximately 100 h. Aside from water adsorption, since the osmotic membrane efficiency of shales is typically low, it is possible that ions are simultaneously allowed in and out. However, the effect of ion movement on shale swelling is lower than water adsorption [82]. It is difficult to replicate formation brines synthetically [29]: pore fluid disequilibrium may cause swelling- or shrinkage-induced damage to shales [83,84]. Osmotic pressure-induced changes caused by significant differences in ionic concentrations close to the clay surfaces and in the pore fluid [85] may thus be triggered. Smectite is predominantly prone to osmotic processes. The difference between synthetic and native pore fluid is, however, assumed to be insignificant with osmotic swelling only playing a minor part in the observed swelling. Moreover, Ewy and Stankovic [86] found that sufficient effective stress prevents chemically induced swelling which is an indication that water adsorption in an undersaturated shale is the main mechanism.

Santos and da Fontoura [87] argued that the observed swelling of laboratory shale specimens comprising all types of clay minerals is caused by surface hydration related to the amount and distribution of water within the shale. Overall electrical neutrality in fluid–clay interaction is maintained by the distribution of the cationic fluid being concentrated at the surface of the anionic clay particle. Universal for all types of clay minerals is the resulting layer named the diffuse double layer (DDL) that may induce swelling because the adsorbed layer thickness surrounding the clay particles increases [88]. Schaefer et al. [89] observed shrinkage of the interlayer spacing at higher hydration states corresponding to shallow burial depths. Compaction turned into expansion at 320 h, whereupon the specimen expanded at a continuously decreasing rate until the end of the experiment. Clay minerals charged with CO<sub>2</sub> experience different levels of swelling depending on their water content and interlayer cations [8]. CO<sub>2</sub> adsorption within the smectite interlayer is believed to be the main contributor causing the observed swelling. CO<sub>2</sub> adsorption capacity may be affected by decompaction during coring. Best fit to in situ adsorption conditions is however ensured because the specimen is at in situ stress conditions before being exposed to CO<sub>2</sub>.

Based on previous studies, Young's modulus and Poisson's ratio [16,20–25,32–34], tensile strength [25–28], and P- and S-wave velocities [25,33,34] generally decrease with CO<sub>2</sub> exposure. Reductions with CO<sub>2</sub> exposure are primarily attributed to adsorption-induced swelling of clay minerals and dissolution-induced pore structure changes primarily affecting calcite but secondarily also feldspar. A common denominator is that these shales are calcite-rich. Exceptions that prove the rule do however exist: constant or increasing Young's modulus and Poisson's ratios [25,29], tensile strength [25,29,30], and P- and S-wave velocities [25]. Dewhurst et al. [29] considered stiffening and strengthening caused by dissolution and re-precipitation of minerals unlikely and instead opted for an explanation involving water loss. It appears as though it depends on whether (i) or not (ii) CO<sub>2</sub> coexists with water or brine: (i) softening and weakening are explained by dissolution being more dominant than precipitation but (ii) stiffening and strengthening are instead attributed to water dehydration. CO<sub>2</sub> and water or brine coexistence implies lower pH. Choi et al. [25] measured both increments and decrements depending on (i) or (ii) being enforced.

$E_V$  and  $\nu_{VH}$  changes at 25 Hz are observed to be minimal irrespective of phase:  $E_V$  is slightly affected and  $\nu_{VH}$  is virtually unaffected (Figure 8). In fact, the overall reduction of  $E_V$  amounts to less than 2% and occurs during Phase (ii) before CO<sub>2</sub> is introduced during Phase (iii). Figure 9 is comparatively different due to  $V_{P_0}$  and  $V_{S_0}$  constantly decreasing during all phases.  $E_V$  is related to  $V_{P_0}$  and  $V_{S_0}$  in the sense that greater stiffness typically implies higher velocities. Temperature outside the sleeve has been recorded in

previous tests but was not a priority in this test due to it being found to only vary by  $\pm 0.25$  °C.  $E_V$  and  $\nu_{VH}$  from hypersensitive strain gauges are more likely to be affected by temperature than  $V_{P_0}$  and  $V_{S_0}$  from piezoceramics if the temperature-elevated mixing unit imposes temperature variations at specimen level. It is, however, unlikely that temperature variations of these small magnitudes would amount to great errors. DT#1 and DT#2 are thought to provide stiffer  $E_V$  responses than DT#3 due to the rapid expansion of our specimen observed until 70 h in Figure 7. Neither stiffening nor weakening appears to affect the seismic dispersion (Figure 10) though. It is, however, unknown whether the dispersion at unprobed frequencies (between seismic and ultrasonic) is affected or also remains unaffected. Dispersion is notably sensitive to fluid mobility: small permeability or viscosity changes could explain seismic  $E_V$  and ultrasonic  $V_{P_0}$  and  $V_{S_0}$  behaving differently. Since it is unobserved at seismic frequencies, the Cole–Cole model (Figure 11) is unaffected. Bound water with finite shear stiffness [90,91] and enhanced viscosity [90,92–94] could also possibly be affected by CO<sub>2</sub>. Other possibilities are differing pH values for the different fluids, amount of diffusion into the shale bulk, associated changes in surface energy, and desiccation effects.

Neither  $E_V$  and  $\nu_{VH}$  nor  $V_{P_0}$  and  $V_{S_0}$  are greatly impacted by the different fluids for reasons that remain unclear. CO<sub>2</sub> was expected to change the properties [95] to a greater extent than what is observed but was perhaps limited due to Draupne's lack of calcite and feldspar (Table 1).  $E_V$  and  $\nu_{VH}$  plus  $V_{P_0}$  and  $V_{S_0}$  are also close to the experimental errors which questions as to whether the changes are physical or artificial. It is, however, an indication that Draupne Shale is suitable for CCS purposes because the changes would not be as negligible if its integrity was greatly impacted. If neither dissolution nor precipitation is dominant but instead they counteract each other, no significant stiffness or strength changes would be observed. Changes in stiffness need not be of the same sign as changes in compressive strength: loss of point cementation at grain contacts with no loss of large volumes of minerals or grains may lead to a weaker bulk but stiffer specimen if finer material is trapped in the pore volume. Time is another aspect to consider because our 24-day experiment is incomparable to in situ timescales. Despite the length scales also being incomparable, diffusion is a notoriously slow process at any scale. Figure 11 is one out of an infinite number of solutions.  $E_H > E_{45} > E_V$  and  $0 < \nu_{HH} < \nu_{HV}$  are criteria that most shales obey although exceptions do exist [96]. The amount of data obtainable from a single specimen is, however, shown. It is by no means any substitution from performing all three experiments (0, 45, and 90° specimens) required for full characterization assuming TI symmetry but it still offers valuable information. In situ caprock shales are also mostly 0° relative to the reservoir rocks they cover.

Interesting is also the duration of this experiment despite being incomparable to in situ timescales. To our knowledge, it is the longest FO experiment with its 575 operational hours. It was also the only known experiment that performed FO measurement as a function of time instead of frequency at its time of completion. Our primary intention is to describe a technique that monitors changes in elastic properties at seismic and ultrasonic frequencies with time. As such, it is analogous to time-lapse (4D) surveillance in the field. Continuous FO and PT measurement over time could also be extended to conventional creep measurements in the absence of CO<sub>2</sub>. Chavez et al. [97] later studied FO-measured creep effects on a limestone, a sandstone, and a shale at 2 Hz but at room-dry and uniaxial conditions. Instead of 575 h, they measured for 120 h. It appears as though they did not consider anisotropy because they did not specify the orientation of their Eagle Ford Shale and only included isotropic calculations. They did, however, specify that the largest observed changes occurred in their shale. These results were later also included in Mikhaltsevitch et al. [71].

## 6. Conclusions

We propose using FO and PT for simultaneous  $E_V$  and  $\nu_{VH}$  as well as  $V_{P_0}$  and  $V_{S_0}$  measurements over an elongated period of time (in the presence and in the absence of CO<sub>2</sub>)

at constant seismic and ultrasonic frequencies. Three successive phases of fluid exposure are implemented without exposing the specimen to ambient conditions between phases during a single 575 h experiment. This method provides a better understanding of in situ versus laboratory measurements because both frequencies are simultaneously probed at in situ pressure conditions despite the omnipresent up-scaling issue. Shale-dehydration that may alter the rock properties as a consequence of exposure to ambient conditions is avoided because pore fluid loss is eliminated (except during the initial mounting). Draupne Shale appears to be resilient to CO<sub>2</sub> exposure as its integrity is neither compromised by notable  $E_V$  and  $\nu_{VH}$  nor  $V_{P_0}$  and  $V_{S_0}$  changes. CO<sub>2</sub> appear to not impact the observed  $E_V$  and  $\nu_{VH}$  dispersion beyond minor amplitude variations with time. These changes are attributed to the initial swelling of the specimen. CO<sub>2</sub> dissolved in brine is acidic and thus prone to primarily dissolve calcite. However, calcite is a diminutive component of Draupne Shale which could explain its resilience to acidic CO<sub>2</sub>-brine. For significant changes to occur in the presence of CO<sub>2</sub>, calcite-rich shale specimens that are poor candidates for CCS purposes need to be tested. This combination of seismic and ultrasonic measurements is, however, useful in proposing a 4D surveillance plan to reservoirs covered by Draupne Shale. Small transient changes in stiffness when CO<sub>2</sub> comes into contact with new sections of caprock could map the progress of the plume front.

**Author Contributions:** Conceptualization, A.B. and P.R.C.; methodology, S.R. and A.B.; formal analysis, S.R. and M.H.B.; investigation, S.R.; writing—original draft preparation, S.R.; writing—review and editing, M.H.B., A.B. and P.R.C.; visualization, S.R.; supervision, A.B. and P.R.C.; project administration, A.B. and P.R.C.; funding acquisition, P.R.C. All authors have read and agreed to the published version of the manuscript.

**Funding:** This research was funded by the ROck SEismic (ROSE) research project (grant number 228400) as part of the scholarship of S.R. The experiment was funded by Stress Path and Hysteresis effects on Integrity of CO<sub>2</sub> Storage Sites (SPHINCCS) (grant number 268445).

**Data Availability Statement:** All experimental measurements are available upon request from the corresponding author.

**Acknowledgments:** We thank SINTEF for granting us access to their Formation Physics Laboratory. We also thank SINTEF employees Jørn F. Stenebråten, Eyvind F. Sønstebo, Andreas N. Berntsen, Lars-Erik Walle, Serhii Lozovyi, Dawid Szewczyk, Anna M. Stroisz, and Nicolaine Agofack for technical support. Three anonymous reviewers are also acknowledged for elevating the quality of this manuscript.

**Conflicts of Interest:** The authors declare no conflict of interest.

## Abbreviations

Abbreviations used in this manuscript by order of appearance:

CO <sub>2</sub>	Carbon Dioxide
CCS	Carbon Capture and Storage
IPCC	International Panel on Climate Change
IPCC	Intergovernmental Panel on Climate Change
NaCl	Sodium Chloride
pH	Potential of Hydrogen
scCO <sub>2</sub>	Supercritical Carbon Dioxide
Ca	Calcium
Na	Sodium
CH <sub>4</sub>	Methane
UCS	Uniaxial Compressive Strength
FO	Forced Oscillation
PT	Pulse Transmission
TI	Transverse Isotropy



LVDTs	Linear Variable Displacement Transducers
KKR	Kramers–Kronig Relations
XRD	X-ray Diffraction
PEEK	Polyetheretherketone
DDL	Diffuse Double Layer

## References

- Metz, B.; Davidson, O.; De Coninck, H.; Loos, M.; Meyer, L. *IPCC Special Report on Carbon Dioxide Capture and Storage*; Cambridge University Press: Cambridge, UK, 2005.
- Torp, T.; Gale, J. Demonstrating storage of CO<sub>2</sub> in geological reservoirs: The Sleipner and SACS projects. *Energy* **2004**, *29*, 1361–1369. [[CrossRef](#)]
- Gislason, S.; Wolff-Boenisch, D.; Stefansson, A.; Oelkers, E.; Gunnlaugsson, E.; Sigurdardottir, H.; Sigfusson, B.; Broecker, W.; Matter, J.; Stute, M.; et al. Mineral sequestration of carbon dioxide in basalt: A pre-injection overview of the CarbFix project. *Int. J. Greenh. Gas Control* **2010**, *4*, 537–545. [[CrossRef](#)]
- Lu, J.; Kharaka, Y.; Thordsen, J.; Horita, J.; Karamalidis, A.; Griffith, C.; Hakala, J.A.; Ambats, G.; Cole, D.; Phelps, T.; et al. CO<sub>2</sub>–rock–brine interactions in Lower Tuscaloosa Formation at Cranfield CO<sub>2</sub> sequestration site, Mississippi, U.S.A. *Chem. Geol.* **2012**, *291*, 269–277. [[CrossRef](#)]
- Wilson, E.; Gerard, D. *Carbon Capture and Sequestration: Integrating Technology, Monitoring, Regulation*; U. S. Department of Energy Office of Scientific and Technical Information: Oak Ridge, TN, USA, 2007.
- Bennaceur, K.; Gielen, D.; Kerre, T.; Tam, C. *CO<sub>2</sub> Capture and Storage: A Key Carbon Abatement Option*; International Energy Agency: Paris, France, 2008; p. 264. [[CrossRef](#)]
- Kampman, N.; Busch, A.; Bertier, P.; Snippe, J.; Hangx, S.; Pipich, V.; Di, Z.; Rother, G.; Harrington, J.; Evans, J.; et al. Observational evidence confirms modelling of the long-term integrity of CO<sub>2</sub>-reservoir caprocks. *Nat. Commun.* **2016**, *7*, 12268. [[CrossRef](#)]
- Busch, A.; Bertier, P.; Gensterblum, Y.; Rother, G.; Spiers, C.; Zhang, M.; Wentinck, H. On sorption and swelling of CO<sub>2</sub> in clays. *Geomech. Geophys. Geo-Energy Geo-Resour.* **2016**, *2*, 111–130. [[CrossRef](#)]
- Wang, Z.; Nur, A. Effects of CO<sub>2</sub> Flooding on Wave Velocities in Rocks With Hydrocarbons. *SPE-17345-PA* **1989**, *4*, 429–436. [[CrossRef](#)]
- Mavko, G.; Mukerji, T.; Dvorkin, J. *The Rock Physics Handbook*; Cambridge university press: Cambridge, UK, 2020.
- Espinoza, D.; Santamarina, J. CO<sub>2</sub> breakthrough—Caprock sealing efficiency and integrity for carbon geological storage. *Int. J. Greenh. Gas Control* **2017**, *66*, 218–229. [[CrossRef](#)]
- Peng, C.; Crawshaw, J.; Maitland, G.; Trusler, J.; Vega-Maza, D. The pH of CO<sub>2</sub>-saturated water at temperatures between 308K and 423K at pressures up to 15MPa. *J. Supercrit. Fluids* **2013**, *82*, 129–137. [[CrossRef](#)]
- Haghi, R.K.; Chapoy, A.; Peirera, L.; Yang, J.; Tohidi, B. pH of CO<sub>2</sub> saturated water and CO<sub>2</sub> saturated brines: Experimental measurements and modelling. *Int. J. Greenh. Gas Control* **2017**, *66*, 190–203. [[CrossRef](#)]
- Gaus, I. Role and impact of CO<sub>2</sub>–rock interactions during CO<sub>2</sub> storage in sedimentary rocks. *Int. J. Greenh. Gas Control* **2010**, *4*, 73–89. [[CrossRef](#)]
- Alemu, B.; Aagaard, P.; Munz, I.; Skurtveit, E. Caprock interaction with CO<sub>2</sub>: A laboratory study of reactivity of shale with supercritical CO<sub>2</sub> and brine. *Appl. Geochem.* **2011**, *26*, 1975–1989. [[CrossRef](#)]
- Choi, C.S.; Song, J.J. *Swelling and Mechanical Property Change of Shale and Sandstone in Supercritical CO<sub>2</sub>*; ISRM-ARMS7-2012-104; International Society for Rock Mechanics and Rock Engineering: Seoul, Korea, 2012; p. 11.
- Busch, A.; Alles, S.; Gensterblum, Y.; Prinz, D.; Dewhurst, D.; Raven, M.; Stanjek, H.; Krooss, B. Carbon dioxide storage potential of shales. *Int. J. Greenh. Gas Control* **2008**, *2*, 297–308. [[CrossRef](#)]
- Dewhurst, D.; Delle Piane, C.; Esteban, L.; Sarout, J.; Josh, M.; Pervukhina, M.; Clennell, M. Microstructural, Geomechanical, and Petrophysical Characterization of Shale Caprocks. In *Geological Carbon Storage Subsurface Seals and Caprock Integrity*; Vialle, S., Ajo-Franklin, J., Carey, J.W., Eds.; Wiley Online Library: Hoboken, NJ, USA, 2019; Chapter 10, pp. 1–30.
- Klewiah, I.; Berawala, D.; Walker, H.; Andersen, P.; Nadeau, P. Review of experimental sorption studies of CO<sub>2</sub> and CH<sub>4</sub> in shales. *J. Nat. Gas Sci. Eng.* **2020**, *73*, 103045. [[CrossRef](#)]
- Lyu, Q.; Ranjith, P.; Long, X.; Ji, B. Experimental Investigation of Mechanical Properties of Black Shales after CO<sub>2</sub>-Water-Rock Interaction. *Materials* **2016**, *9*, 663. [[CrossRef](#)]
- Zhang, S.; Xian, X.; Zhou, J.; Zhang, L. Mechanical behaviour of Longmaxi black shale saturated with different fluids: An experimental study. *RSC Adv.* **2017**, *7*, 42946–42955. [[CrossRef](#)]
- Yin, H.; Zhou, J.; Xian, X.; Jiang, Y.; Lu, Z.; Tan, J.; Liu, G. Experimental study of the effects of sub-and super-critical CO<sub>2</sub> saturation on the mechanical characteristics of organic-rich shales. *Energy* **2017**, *132*, 84–95. [[CrossRef](#)]
- Lyu, Q.; Long, X.; Ranjith, P.; Tan, J.; Kang, Y.; Wang, Z. Experimental investigation on the mechanical properties of a low-clay shale with different adsorption times in sub-/super-critical CO<sub>2</sub>. *Energy* **2018**, *147*, 1288–1298. [[CrossRef](#)]
- Lu, Y.; Chen, X.; Tang, J.; Li, H.; Zhou, L.; Han, S.; Ge, Z.; Xia, B.; Shen, H.; Zhang, J. Relationship between pore structure and mechanical properties of shale on supercritical carbon dioxide saturation. *Energy* **2019**, *172*, 270–285. [[CrossRef](#)]
- Choi, C.S.; Kim, J.; Song, J.J. Analysis of shale property changes after geochemical interaction under CO<sub>2</sub> sequestration conditions. *Energy* **2021**, *214*, 118933. [[CrossRef](#)]

26. Ao, X.; Lu, Y.; Tang, J.; Chen, Y.; Li, H. Investigation on the physics structure and chemical properties of the shale treated by supercritical CO<sub>2</sub>. *J. CO<sub>2</sub> Util.* **2017**, *20*, 274–281. [[CrossRef](#)]
27. Zou, Y.; Li, S.; Ma, X.; Zhang, S.; Li, N.; Chen, M. Effects of CO<sub>2</sub>-brine-rock interaction on porosity/permeability and mechanical properties during supercritical-CO<sub>2</sub> fracturing in shale reservoirs. *J. Nat. Gas Sci. Eng.* **2018**, *49*, 157–168. [[CrossRef](#)]
28. Feng, G.; Kang, Y.; Sun, Z.D.; Wang, X.C.; Hu, Y.Q. Effects of supercritical CO<sub>2</sub> adsorption on the mechanical characteristics and failure mechanisms of shale. *Energy* **2019**, *173*, 870–882. [[CrossRef](#)]
29. Dewhurst, D.; Raven, M.; Shah, S.; Ali, S.; Giwelli, A.; Firns, S.; Josh, M.; White, C. Interaction of super-critical CO<sub>2</sub> with mudrocks: Impact on composition and mechanical properties. *Int. J. Greenh. Gas Control* **2020**, *102*, 103163. [[CrossRef](#)]
30. Ojala, I. The effect of CO<sub>2</sub> on the mechanical properties of reservoir and cap rock. *Energy Procedia* **2011**, *4*, 5392–5397. [[CrossRef](#)]
31. Bhuiyan, M.; Agofack, N.; Gawel, K.; Cerasi, P. Micro-and Macroscale Consequences of Interactions between CO<sub>2</sub> and Shale Rocks. *Energies* **2020**, *13*, 1167. [[CrossRef](#)]
32. Agofack, N.; Cerasi, P.; Stroisz, A.; Rørheim, S. *Sorption of CO<sub>2</sub> and Integrity of Caprock Shale*; ARMA-2019-257; American Rock Mechanics Association: New York, NY, USA, 2019; p. 9.
33. Al-Ameri, W.; Abdurraheem, A.; Mahmoud, M. Long-term effects of CO<sub>2</sub> sequestration on rock mechanical properties. *J. Energy Resour. Technol.* **2016**, *138*, 012201. [[CrossRef](#)]
34. Elwegaa, K.; Emadi, H.; Soliman, M.; Gamadi, T.; Elsharafi, M. Improving oil recovery from shale oil reservoirs using cyclic cold carbon dioxide injection—An experimental study. *Fuel* **2019**, *254*, 115586. [[CrossRef](#)]
35. Lebedev, M.; Pervukhina, M.; Mikhaltsevitch, V.; Dance, T.; Bilenko, O.; Gurevich, B. An experimental study of acoustic responses on the injection of supercritical CO<sub>2</sub> into sandstones from the Otway Basin. *Geophysics* **2013**, *78*, D293–D306. [[CrossRef](#)]
36. Fatah, A.; Bennour, Z.; Ben Mahmud, H.; Gholami, R.; Hossain, M. A Review on the Influence of CO<sub>2</sub>/Shale Interaction on Shale Properties: Implications of CCS in Shales. *Energies* **2020**, *13*, 3200. [[CrossRef](#)]
37. Skurtveit, E.; Grande, L.; Ogebule, O.; Gabrielsen, R.; Faleide, J.; Mondol, N.; Maurer, R.; Horsrud, P. *Mechanical Testing and Sealing Capacity of the Upper Jurassic Draupne Formation, North Sea*; ARMA-2015-331; American Rock Mechanics Association: San Francisco, CA, USA, 2015; p. 8.
38. Zadeh, M.; Mondol, N.; Jahren, J. Velocity anisotropy of Upper Jurassic organic-rich shales, Norwegian Continental Shelf. *Geophysics* **2017**, *82*, C61–C75. [[CrossRef](#)]
39. Mondol, N. *Geomechanical and Seismic Behaviors of Draupne Shale: A Case Study from the Central North Sea*; European Association of Geoscientists and Engineers: London, UK, 2019; p. 4. [[CrossRef](#)]
40. Nakagawa, S.; Kneafsey, T.; Daley, T.; Freifeld, B.; Rees, E. Laboratory seismic monitoring of supercritical CO<sub>2</sub> flooding in sandstone cores using the Split Hopkinson Resonant Bar technique with concurrent X-ray computed tomography imaging. *Geophys. Prospect.* **2013**, *61*, 254–269. [[CrossRef](#)]
41. Mikhaltsevitch, V.; Lebedev, M.; Gurevich, B. Measurements of the elastic and anelastic properties of sandstone flooded with supercritical CO<sub>2</sub>. *Geophys. Prospect.* **2014**, *62*, 1266–1277. [[CrossRef](#)]
42. Tisato, N.; Quintal, B.; Chapman, S.; Podladchikov, Y.; Burg, J.P. Bubbles attenuate elastic waves at seismic frequencies: First experimental evidence. *Geophys. Res. Lett.* **2015**, *42*, 3880–3887. [[CrossRef](#)]
43. Spencer, J.; Shine, J. Seismic wave attenuation and modulus dispersion in sandstones. *Geophysics* **2016**, *81*, D211–D231. [[CrossRef](#)]
44. Massaad, J. The Effect of Partial CO<sub>2</sub> Saturation on the Elastic Properties of Castlegate Sandstone Measured at Seismic and Ultrasonic Frequencies. Master's Thesis, NTNU, Trondheim, Norway, 2016.
45. Agofack, N.; Lozovyi, S.; Bauer, A. Effect of CO<sub>2</sub> on P- and S-wave velocities at seismic and ultrasonic frequencies. *Int. J. Greenh. Gas Control* **2018**, *78*, 388–399. [[CrossRef](#)]
46. Voigt, W. *Lehrbuch der Kristallphysik: (Mit Ausschluss der Kristalloptik)*; B.G. Teubners Sammlung von Lehrbüchern auf dem Gebiete der Mathematischen Wissenschaften; B.G. Teubner: Wiesbaden, Germany, 1910.
47. Hooke, R. *De Potentia Restitutiva*; John Martyn: London, UK, 1678.
48. Thomsen, L. Weak elastic anisotropy. *Geophysics* **1986**, *51*, 1954–1966. [[CrossRef](#)]
49. Spencer, J. Stress relaxations at low frequencies in fluid-saturated rocks: Attenuation and modulus dispersion. *J. Geophys. Res. Solid Earth* **1981**, *86*, 1803–1812. [[CrossRef](#)]
50. Cole, K.; Cole, R. Dispersion and Absorption in Dielectrics I. Alternating Current Characteristics. *J. Chem. Phys.* **1941**, *9*, 341–351. [[CrossRef](#)]
51. Debye, P. *Polar Molecules*; The Chemical Catalog Company: New York, NY, USA, 1929.
52. Kronig, R. On the theory of dispersion of x-rays. *J. Opt. Soc. Am.* **1926**, *12*, 547–557. [[CrossRef](#)]
53. Kramers, H. La diffusion de la lumière par les atomes. *Atti Cong. Intern. Fisica Trans. Volta Centen. Congr. Como* **1927**, *2*, 545–557.
54. Batzle, M.; Han, D.H.; Hofmann, R. Fluid mobility and frequency-dependent seismic velocity - Direct measurements. *Geophysics* **2006**, *71*, N1–N9. [[CrossRef](#)]
55. Szewczyk, D.; Bauer, A.; Holt, R. Stress-dependent elastic properties of shales—laboratory experiments at seismic and ultrasonic frequencies. *Geophys. J. Int.* **2018**, *212*, 189–210. [[CrossRef](#)]
56. Tutuncu, A.; Podio, A.; Gregory, A.; Sharma, M. Nonlinear viscoelastic behavior of sedimentary rocks, Part I: Effect of frequency and strain amplitude. *Geophysics* **1998**, *63*, 184–194. [[CrossRef](#)]
57. Fjær, E.; Holt, R.; Raaen, A.; Horsrud, P. *Petroleum Related Rock Mechanics*; Elsevier: Amsterdam, The Netherlands, 2008.

58. Szewczyk, D.; Bauer, A.; Holt, R. A new laboratory apparatus for the measurement of seismic dispersion under deviatoric stress conditions. *Geophys. Prospect.* **2016**, *64*, 789–798. [[CrossRef](#)]
59. Hughes, D.; Pondrom, W.; Mims, R. Transmission of Elastic Pulses in Metal Rods. *Phys. Rev.* **1949**, *75*, 1552–1556. [[CrossRef](#)]
60. Birch, F. The velocity of compressional waves in rocks to 10 kilobars: 1. *J. Geophys. Res. (1896–1977)* **1960**, *65*, 1083–1102. [[CrossRef](#)]
61. Toksöz, M.; Johnston, D.; Timur, A. Attenuation of seismic waves in dry and saturated rocks: I. Laboratory measurements. *Geophysics* **1979**, *44*, 681–690. [[CrossRef](#)]
62. Winkler, K. Frequency dependent ultrasonic properties of high-porosity sandstones. *J. Geophys. Res. Solid Earth* **1983**, *88*, 9493–9499. [[CrossRef](#)]
63. Lozovyi, S.; Bauer, A. Velocity dispersion in rocks: A laboratory technique for direct measurement of P-wave modulus at seismic frequencies. *Rev. Sci. Instrum.* **2019**, *90*, 024501. [[CrossRef](#)] [[PubMed](#)]
64. Wheatstone, C. An Account of Several New Processes for Determining the Constants of a Voltaic Circuit. *R. Soc.* **1843**, *4*, 469–471. [[CrossRef](#)]
65. Adam, L.; Batzle, M.; Lewallen, K.; van Wijk, K. Seismic wave attenuation in carbonates. *J. Geophys. Res. Solid Earth* **2009**, *114*. [[CrossRef](#)]
66. Young, T. *A Course of Lectures on Natural Philosophy and the Mechanical Arts: In Two Volumes*; Johnson: London, UK, 1807; Volume 2.
67. Poisson, S. Note sur l'extension des fils et des plaques élastiques. *Ann. Chim. Phys.* **1827**, *36*, 384–387.
68. Lakes, R. *Viscoelastic Materials*; Cambridge University Press: Cambridge, UK, 2009. [[CrossRef](#)]
69. Delle Piane, C.; Sarout, J.; Madonna, C.; Saenger, E.H.; Dewhurst, D.N.; Raven, M. Frequency-dependent seismic attenuation in shales: Experimental results and theoretical analysis. *Geophys. J. Int.* **2014**, *198*, 504–515. [[CrossRef](#)]
70. Huang, Q.; Han, D.H.; Li, H. Laboratory measurement of dispersion and attenuation in the seismic frequency. In *SEG Technical Program Expanded Abstracts 2015*; Society of Exploration Geophysicists (SEG): New Orleans, LA, USA, 2015; pp. 3090–3094.
71. Mikhaltsevitch, V.; Lebedev, M.; Chavez, R.; Vargas, E.; Vasquez, G. A Laboratory Forced-Oscillation Apparatus for Measurements of Elastic and Anelastic Properties of Rocks at Seismic Frequencies. *Front. Earth Sci.* **2021**, *9*, 155. [[CrossRef](#)]
72. Mikhaltsevitch, V.; Lebedev, M.; Pervukhina, M.; Gurevich, B. Seismic dispersion and attenuation in Mancos shale – laboratory measurements. *Geophys. Prospect.* **2021**, *69*, 568–585. [[CrossRef](#)]
73. Szewczyk, D. Frequency Dependent Elastic Properties of Shales—Impact of Partial Saturation and Stress Changes. Ph.D. Thesis, Norwegian University of Science and Technology (NTNU), Trondheim, Norway, 2017.
74. Lozovyi, S. Seismic Dispersion and the Relation between Static and Dynamic Stiffness of Shales. Ph.D. Thesis, Norwegian University of Science and Technology (NTNU), Trondheim, Norway, 2018.
75. Liu, H.P.; Peselnick, L. Investigation of internal friction in fused quartz, steel, plexiglass, and westerly granite from 0.01 to 1.00 Hertz at  $10^{-6}$  to  $10^{-7}$  strain amplitude. *J. Geophys. Res. Solid Earth* **1983**, *88*, 2367–2379. [[CrossRef](#)]
76. Rørheim, S.; Holt, R. How to avoid pitfalls in laboratory measured seismic attenuation. In *AGU Fall Meeting Abstracts*; American Geophysical Union (AGU): San Francisco, CA, USA, 2019; p. 1.
77. Szewczyk, D.; Holt, R.; Bauer, A. Influence of subsurface injection on time-lapse seismic: Laboratory studies at seismic and ultrasonic frequencies. *Geophys. Prospect.* **2018**, *66*, 99–115. [[CrossRef](#)]
78. Rahman, M.; Fawad, M.; Mondol, N. Organic-rich shale caprock properties of potential CO<sub>2</sub> storage sites in the northern North Sea, offshore Norway. *Mar. Pet. Geol.* **2020**, *122*, 104665. [[CrossRef](#)]
79. Rørheim, S.; Bauer, A.; Holt, R. On The Low-Frequency Elastic Response of Pierre Shale During Temperature Cycles. *Geophys. J. Int.* **2021**, submitted.
80. Rørheim, S.; Bauer, A.; Holt, R. On Experimentally Determined Seismic Dispersion and Attenuation—Pierre Shale Measurements and Review. Unpublished.
81. Yan, F.; Han, D.H.; Yao, Q. Physical constraints on C<sub>13</sub> and δ for transversely isotropic hydrocarbon source rocks. *Geophys. Prospect.* **2015**, *64*, 1524–1536. [[CrossRef](#)]
82. Ewy, R. Shale swelling/shrinkage and water content change due to imposed suction and due to direct brine contact. *Acta Geotech.* **2014**, *9*, 869–886. [[CrossRef](#)]
83. Ewy, R. Shale/claystone response to air and liquid exposure, and implications for handling, sampling and testing. *Int. J. Rock Mech. Min. Sci.* **2015**, *80*, 388–401. [[CrossRef](#)]
84. Ewy, R. Practical approaches for addressing shale testing challenges associated with permeability, capillarity and brine interactions. *Geomech. Energy Environ.* **2018**, *14*, 3–15. [[CrossRef](#)]
85. Lal, M. *Shale Stability: Drilling Fluid Interaction and Shale Strength*; SPE-54356-MS; Society of Petroleum Engineers (SPE): Caracas, Venezuela, 1999; p. 10. [[CrossRef](#)]
86. Ewy, R.; Stankovic, R. Shale swelling, osmosis, and acoustic changes measured under simulated downhole conditions. *SPE Drill. Complet.* **2010**, *25*, 177–186. [[CrossRef](#)]
87. Santos, H.; da Fontoura, S. *Concepts and Misconceptions of Mud Selection Criteria: How to Minimize Borehole Stability Problems?* SPE-38644-MS; Society of Petroleum Engineers (SPE): San Antonio, CA, USA, 1997; p. 16. [[CrossRef](#)]
88. Puppala, A.; Pedarla, A.; Pino, A.; Hoyos, L. Diffused Double-Layer Swell Prediction Model to Better Characterize Natural Expansive Clays. *J. Eng. Mech.* **2017**, *143*, 04017069. [[CrossRef](#)]

89. Schaef, H.; Ilton, E.; Qafoku, O.; Martin, P.; Felmy, A.; Rosso, K. In situ XRD study of Ca<sup>2+</sup> saturated montmorillonite (STX-1) exposed to anhydrous and wet supercritical carbon dioxide. *Int. J. Greenh. Gas Control* **2012**, *6*, 220–229. [[CrossRef](#)]
90. Antognozzi, M.; Humphris, A.; Miles, M. Observation of molecular layering in a confined water film and study of the layers viscoelastic properties. *Appl. Phys. Lett.* **2001**, *78*, 300–302. [[CrossRef](#)]
91. Holt, R.; Kolstø, M. How does water near clay mineral surfaces influence the rock physics of shales? *Geophys. Prospect.* **2017**, *65*, 1615–1629. [[CrossRef](#)]
92. Major, R.; Houston, J.; McGrath, M.; Siepmann, J.; Zhu, X.Y. Viscous water meniscus under nanoconfinement. *Phys. Rev. Lett.* **2006**, *96*, 177803. [[CrossRef](#)]
93. Goertz, M.; Houston, J.; Zhu, X.Y. Hydrophilicity and the viscosity of interfacial water. *Langmuir* **2007**, *23*, 5491–5497. [[CrossRef](#)]
94. Ulcinas, A.; Valdre, G.; Snitka, V.; Miles, M.; Claesson, P.; Antognozzi, M. Shear response of nanoconfined water on muscovite mica: Role of cations. *Langmuir* **2011**, *27*, 10351–10355. [[CrossRef](#)] [[PubMed](#)]
95. Prasad, M.; Glubokovskikh, S.; Daley, T.; Oduwole, S.; Harbert, W. CO<sub>2</sub> messes with rock physics. *Lead. Edge* **2021**, *40*, 424–432. [[CrossRef](#)]
96. Sarout, J. Comment on “Physical constraints on C<sub>13</sub> and δ for transversely isotropic hydrocarbon source rocks” by F. Yan, D.-H. Han and Q. Yao, *Geophysical Prospecting* **2016**, *65*, 393–411. *Geophys. Prospect.* **2016**, *65*, 379–380. [[CrossRef](#)]
97. Chavez, R.; Mikhailsevitch, V.; Lebedev, M.; Gurevich, B.; Vargas, E.; Vasquez, G. Influence of the Creep Effect on the Low-Frequency Measurements of the Elastic Moduli of Sedimentary Rocks. In Proceedings of the 81st EAGE Conference and Exhibition 2019, London, UK, 3–6 June 2019; European Association of Geoscientists & Engineers (EAGE): London, UK, 2019; Volume 2019, pp. 1–6.